

Results of an Aeroelastically Tailored Wing on the FLEXOP Demonstrator Aircraft

Roessler, Christian; Teubl, Daniel; Meddaikar, Yasser; Wüstenhagen, Matthias; Ossmann, Daniel; Sodja, Jurij; De Breuker, Roeland; Luspay, Tamás; Gyulai, László; More Authors

DOI

[10.2514/6.2020-1969](https://doi.org/10.2514/6.2020-1969)

Publication date

2020

Document Version

Final published version

Published in

AIAA Scitech 2020 Forum

Citation (APA)

Roessler, C., Teubl, D., Meddaikar, Y., Wüstenhagen, M., Ossmann, D., Sodja, J., De Breuker, R., Luspay, T., Gyulai, L., & More Authors (2020). Results of an Aeroelastically Tailored Wing on the FLEXOP Demonstrator Aircraft. In *AIAA Scitech 2020 Forum: 6-10 January 2020, Orlando, FL* (pp. 1-22). [AIAA 2020-1969] (AIAA Scitech 2020 Forum; Vol. 1 PartF). American Institute of Aeronautics and Astronautics Inc. (AIAA). <https://doi.org/10.2514/6.2020-1969>

Important note

To cite this publication, please use the final published version (if applicable).
Please check the document version above.

Copyright

Other than for strictly personal use, it is not permitted to download, forward or distribute the text or part of it, without the consent of the author(s) and/or copyright holder(s), unless the work is under an open content license such as Creative Commons.

Takedown policy

Please contact us and provide details if you believe this document breaches copyrights.
We will remove access to the work immediately and investigate your claim.



Results of an Aeroelastically Tailored Wing on the FLEXOP Demonstrator Aircraft

Christian Roessler¹, Julius Bartasevicius¹, Sebastian J. Koeberle¹, Daniel Teubl¹, Mirko Hornung²
Technical University of Munich, Institute of Aircraft Design, Boltzmannstraße 15, Garching/München, 85748, Germany

Yasser M. Meddaikar³, Johannes K. S. Dillinger³, Wolf R. Krüger⁴
German Aerospace Center DLR-Institute of Aeroelasticity, Göttingen, Lower Saxony, 37073, Germany

Matthias Wüstenhagen⁵, Daniel Ossmann⁵, Thiemo Kier⁵, Gertjan Looye⁶
German Aerospace Center DLR-Institute of System Dynamics and Control, Wessling, 82234, Germany

Jurij Sodja⁷, Roeland de Breuker⁸
Delft University of Technology, Delft, South-Holland, 2629HS, The Netherlands

Tamás Luspay⁹, László Gyulai⁹, Dániel Balogh⁹, Bálint Vanek¹⁰
MTA SZTAKI – Hungarian Academy of Science, Budapest, 1111, Hungary

Panagiotis Georgopoulos¹¹, Dr. Christos Koimtzoglou¹²
INASCO Hellas Co, 18 Napoleontos Zerva str, Glyfada, Athens, 16675, Greece

The idea of the EU funded FLEXOP project is to raise efficiency of a currently existing wing by derivative solution with higher aspect ratio at no excess structural weight. In order to enable such a resulting highly flexible wing the project goal is to develop methods for active suppression of flutter and passive load alleviation. The developed methods will be tested and validated with a UAV flutter demonstrator. The demonstrator is a 7m wingspan, 65kg MTOW UAV equipped with a jet engine. It features three different wing pairs. The first wing is a stiff design reference case, which is flown to get the baseline measurements for comparison. The second one is a wing designed very flexible specifically for active flutter control. The third wing is aeroelastically tailored for gust load alleviation. The paper describes the results of the aeroelastically tailored wing compared to the baseline reference wing.

I. Introduction

Flutter Free FLight Envelope eXpansion for ecOnomic Performance improvement (FLEXOP) is a project within the European Union's Horizon 2020 framework. Its main goal is to raise efficiency of a currently existing wing by derivative solution with higher aspect ratio at no excess structural weight. The benefit of increased span will be increased lift to drag ratio and therefore less fuel burn. This should be accomplished ideally with no mass penalty. The

¹ Research Associate, Institute of Aircraft Design

² Professor, Head of the Institute of Aircraft Design

³ Research Scientist, Loads Analysis and Aeroelastic Design

⁴ Department Leader, Loads Analysis and Aeroelastic Design

⁵ Research Scientist, Aircraft System Dynamics

⁶ Head of Department, Aircraft System Dynamics

⁷ Senior Scientist, Faculty of Aerospace Engineering, Aerospace Structures and Computational Mechanics

⁸ Associate Professor, Faculty of Aerospace Engineering, Aerospace Structures and Computational Mechanics

⁹ Research Fellow, Computer and Automation Research Institute

¹⁰ Senior Research Fellow, Systems and Control Lab

¹¹ Aerospace Engineer

¹² Managing Director

downside of the more slender lightweight wings is their higher flexibility which arises the problems of aeroelasticity. Especially flutter speed will be lower than for a more rigid wing. Therefore very accurate methods for flexible mode modelling and robust flutter control synthesis should be developed within FLEXOP with the aim to fly at the same speed as the baseline aircraft with the enabling features of active flutter control and passive load alleviation to reduce the increased loads on higher aspect ratio wings. The developed methods will be validated with a UAV flutter demonstrator. The 7m span, 65 kg TOW demonstrator will feature three different set of wings: One baseline rigid wing (-0), one wing designed for passive load alleviation (-2) and one very flexible wing (-1) to test active flutter control [1]. After validating the methods and tools the potential of those technologies should be evaluated within a scale up study. Over Airbus XRF1 reference aircraft model, the potential of either 20% payload increase or 7% improvement in fuel efficiency is expected [2].



Figure 1: FLEXOP Demonstrator UAV [3]

This paper focuses on the comparison between baseline and aeroelastically tailored wing. First an overview of the design methods, results and theoretical improvements of the aeroelastically tailored wing is given. Next the planned and conducted flight tests are described including the maneuvers selected for load alleviation testing. An important aspect of flight testing are the required sensors for data gathering. All wings have been equipped with a fiber bragg grating (FBG) system to measure strains during flight testing. Additionally inertia measurement units (IMU) are installed in the wing. While the strain measurement is used to calculate bending moments, shear forces and the wing shape during the test maneuvers, the accelerometers main purpose is for active flutter control. To enhance the precision of the test maneuvers and hence improve data quality an autopilot was developed. With this setup 6 test flights with wing -0 and one with -2 have been completed so far. From those flights first results in terms of flight mechanics, bending moments, shear forces and wing shapes have been evaluated.

II. Design of the wings

Within the FLEXOP project two wing designs are derived to demonstrate the benefits of aeroelastic composite tailoring. The first design, referred to as the reference wing, serves as the baseline. It is derived using the more conventional balanced-symmetric laminates. In contrast to the reference wing, the second design, referred to as the tailored wing, is derived using unbalanced laminates, thus allowing a much larger design space and exploitation of composite coupling benefits. Both wings are optimized to obtain the best possible design given the applied constraints. This allows for a more conservative and realistic assessment of tailoring benefits. In order to impose similar performance constraints on both wings a 1g flight shape was added as an additional constraint. Flight shape in cruise was defined in the form of imposed cruise twist of the two wings.

The design and optimization of the two wings has been previously detailed in [4],[5] and [6] and is briefly described here for the sake of completeness.

The aeroelastic tailoring approach applied in this work is essentially a multi-fidelity procedure where the wing structure is optimized using an aeroelastic tailoring toolchain, developed at the Delft University of Technology (TUD) and DLR-Institute of Aeroelasticity (DLR). In the first step, a beam-model based stiffness-optimization tool PROTEUS [4], [7] and [8] is used to perform initial design-studies and to explore the vast design-space. The optimized design from this step serves as the initial design for the second step in the toolchain. In the second step, a high-fidelity shell-model based genetic algorithm (GA) for stacking sequence optimization [5],[9] and [10] is applied in order to obtain final manufacturing stacking sequence tables.

The objective of the design optimization is to minimize the structural mass of the conceived wings. To maintain a large enough design space while considering ease of manufacturability, the wing is split into 12×1 spanwise and chord-wise design regions. The laminate stacking sequence in the upper and lower skin, and the front and the rear spar is optimized per design region while the laminates in the ribs are pre-defined. Additionally, the leading edge, trailing edge and flaps are not a part of the optimization exercise since they do not belong to the primary structure of the wing.

To obtain a valid performance comparison between the reference and the tailored wing, a constraint on the 1g cruise shape is enforced in the optimization. This way it is ensured that the benefits due to aeroelastic tailoring do not compromise the aerodynamic performance of the designed wings. A linear twist distribution with 0° at the root and -2° at the tip, at 1g cruise is used as the 1g constraint. The optimization objectives, responses and load-cases are summarized in Table 1.

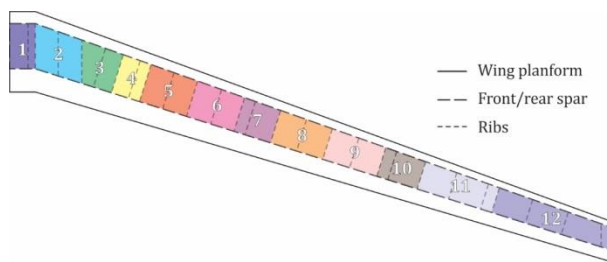


Figure 2 Distribution of wing design regions

Table 1: Aeroelastic tailoring objectives and constraints

Optimization parameter	Value
objective	mass – minimization
outputs	blended stacking sequence jig-twist
physical constraints	laminate strength buckling tip-twist (at 1g cruise) static divergence aileron effectiveness, $\eta > 15\%$
laminate constraints	10% rule [] symmetry ply contiguity (max. 4) $\pm 45^\circ$ outer plies max. disorientation of 45° balance (for reference wing)
sizing load cases	+5g at 45m/S (TAS) -2g at 45m/s (TAS)

The final mass of the reference and the tailored wings is listed in Table 2, detailing the mass obtained in the two steps of the optimization toolchain – the stiffness optimization and the stacking sequence optimization. The tailored wing is almost 8% lighter than the reference in terms of structural mass. This weight saving is solely due to the relaxed laminate definition offered by the unbalanced laminates which allow for extension-shear and bend-twist couplings. The difference between the reference and the tailored wing in terms of stiffness distribution is illustrated in Figure 3 showing the polar distribution of the A_{11} term of the in-plane stiffness matrix in the upper skin. The highly anisotropic stiffness distribution in the tailored wing facilitates the bend-twist coupling that induces a wash-out effect upon increased aerodynamic loading as illustrated in Figure 4a. The wash-out redistributes the aerodynamic loads toward the inboard section of the wing depicted in Figure 4b. As a result, the root bending moments are alleviated. In a 5g and -2g maneuver the tailored wing experiences 6% and 11% lower root bending moments relative to the reference wing. The results for each load case are also summarized in Table 2.

Table 2: Optimized mass and root-bending moment comparison for the reference and tailored wing design

	Mass (kg)	Root bending moment (Nm)		
		1g	5g	-2g
Stiffness-opt. [†] (reference)	5.884	304	1662	726
Stiffness-opt. [†] (tailored)	5.652 (0.96)	305 (1.00)	1555 (0.94)	647 (0.89)
Stacking seq. [‡] (reference)	6.878	310.95	1697.65	-729.61
Stacking seq. [‡] (tailored)	6.307 (0.92)	314.17 (1.01)	1651.86 (0.97)	-689.01 (0.94)

[†]PROTEUS optimization step

[‡]Stacking sequence optimization step

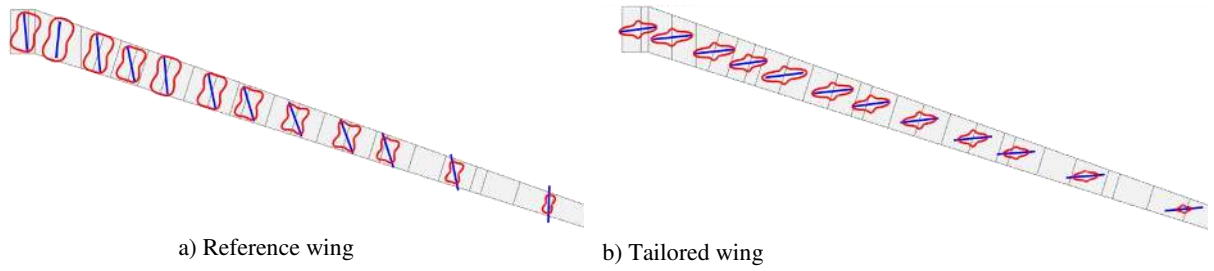


Figure 3: Polar distribution of the in-plane stiffness in the upper skin of the reference and tailored wing

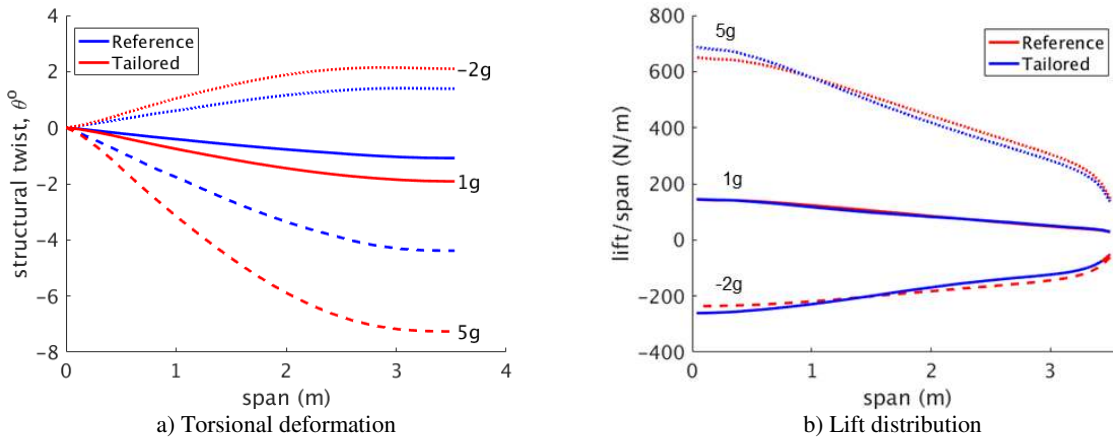


Figure 4: Spanwise torsional deformation and lift distribution for the reference and the tailored wing at selected maneuver loads

The reduced loads result in lesser thickness requirements as shown in Figure 5, leading to the savings in weight. The stiffness, thickness, twist and lift distribution shown correspond to the stacking sequence design.

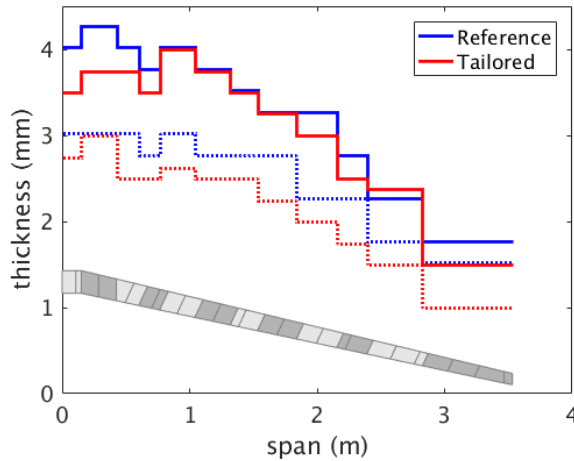


Figure 5: Spanwise laminate thickness distribution in the upper and bottom wing skin

III. FLEXOP UAV Flight Testing and Instrumentation

A. Load Alleviation flight Testing

1. Flight test campaign

A key part of the FLEXOP project is the validation of the developed methods with data conducted from flight tests with the demonstrator. After designing, manufacturing and testing the demonstrator on ground [6] and [11] the flight test could finally be conducted. In preparation operational procedures for flight testing have been compiled and the flight test crew has been trained with a simulator developed by DLR-SR which proved to be very valuable.

The Flight test campaign itself was divided into 4 phases (Figure 6)

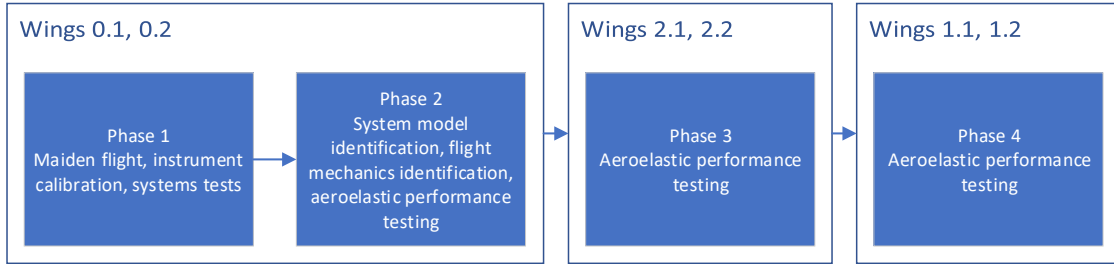


Figure 6: Phases of the flight test campaign

The first and second phases of the flight test campaign dealt with gathering data with the baseline (-0) wing. For the third phase the aeroelastic wing (-2) was mounted for load alleviation testing. Unfortunately phase 4 with the flexible wing (-1) with the final goal of controller based flutter suppression could not be conducted in the scope of the project any more due to time constraints.

All the test flights took place at Special Airport Oberpfaffenhofen. Due to German law, they had to be performed under visual line of sight in a controlled airspace [12]. The map with the marked features (allowed airspace, pilot (PIC) and ground control station (GCS) positions) can be found in Figure 7. The marked airspace is 2280m in length and 620m in width.

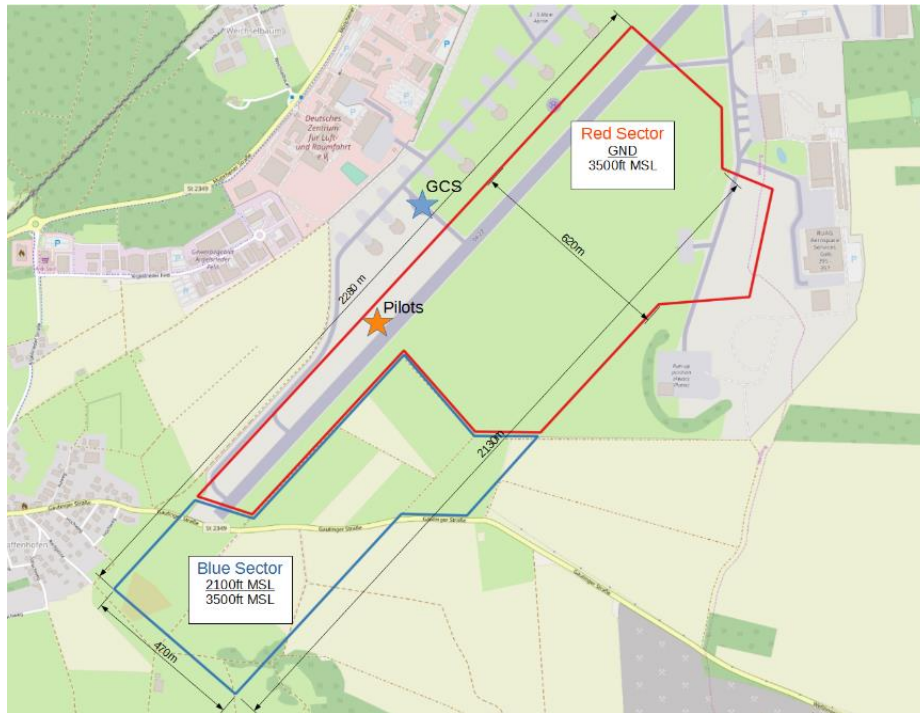


Figure 7. Allowed airspace for testing at EDMO airport.

From the 15 planned test flights for phase one and two with the reference wing (-0) only 5 were conducted and many test points had to be skipped due to time constraints at the end of the project. Static aeroelastic testing manoeuvres, aircraft dynamic performance identification manoeuvres, as well as autopilot functionality (baseline controller) checks were all done at least once (Table 3). All of the aircraft systems were tested and performed as expected.

Table 3. Summary of wing -0 flight tests.

Date	Flight Number	Test Objective	Success?
01.08.2019	1.1	First flight. System and control checks. Airbrake check. Air data system calibration. Flight mechanics check.	Yes
06.08.2019	1.2	Air data system calibration. Flight mechanics check. Familiarization with the aircraft for the second pilot.	Yes
16.10.2019	1.3	Autopilot feed-through mode check. Flight model identification. Airspeed calibration. Aeroelastic tests.	No
23.10.2019	1.4	Aeroelastic tests. Pushover-pullup manoeuvres.	Yes
06.11.2019	1.5	Autopilot baseline controller check. Aeroelastic tests.	Yes

For phase 3 with the aeroelastically tailored wing (-2) 4 flights were planned. However, due to flight testing being one of the last tasks in the project, a very limited time was available for testing the -2.2 wing. In addition, the weather in November got worse and not all days were suitable for flying anymore. The first and only flight was done on 19.11.2019. 22min of flight time were gathered and good quality data of aeroelastic manoeuvres was acquired (Table 4).

Table 4. Summary of wing -2 flight tests.

Date	Flight Number	Test Objective	Success?
19.11.2019	2.1	Maiden flight with -2.2 wing. Testing of baseline controller for using on -2 wing. Turns with increasing bank angle. Pushover-pull-up manoeuvres.	Yes

2. Selection of maneuvers for aeroelastic flight tests

Two flight manoeuvres, a sustained turn at constant bank angle and a pull-up-push-over manoeuvre were selected to be executed during the flight-testing campaign in order to demonstrate passive load alleviation mechanism due to aeroelastic tailoring and to perform the validation of aeroelastic tailoring toolchain developed by TUD and DLR-AE [13],[14].

The sustained turn at constant bank angle was chosen for two reasons. First, the aircraft had to be flown in line-of-sight within a certain flight perimeter and altitude. With these limitations in mind, the sustained turn can be performed at constant velocity for as long as necessary to collect enough data for subsequent analysis. Second, the load factor during such a manoeuvre strongly depends on the bank angle of the turn. Therefore, various load factors can be easily tested by simply adjusting the bank angle of the turn. The sustained turns were defined using the following relation between the desired load factor and the required bank angle:

$$n = 1/\cos(\theta)$$

where θ and n represent the bank angle of the turn and the resulting load factor. Given the flight velocity, v , the turn radius of the manoeuvre is estimated as:

$$r = \frac{v^2}{g n \sin(\theta)}$$

where $g = 9.81 \text{ m/s}^2$ represents the gravitational acceleration. Using these relations, a set of sustained turns at various flight speeds was considered as summarised in Table 5. The maximum turn radius was limited to $r_{\max} = 310 \text{ m}$ by the flight perimeter boundary. One can observe that sustained turns at bank angles of 40 deg, 50 deg and

60 deg at flight speed of 45 m/s fit well within the flight perimeter boundary. Sustained turns with these settings were therefore chosen for flight testing.

Table 5: Summary of sustained turn manoeuvres at various bank angles

Bank angle, θ , [deg]	Load factor, n , [g]	Turn radius, r , [m]		
		$v = 35 \text{ m/s}$	$v = 45 \text{ m/s}$	$v = 55 \text{ m/s}$
0	1.00	-	-	-
15	1.04	466	770	1151
40	1.31	149	246	368
50	1.56	105	173	259
60	2.00	72	119	178
75	3.86	34	55	83

The second manoeuvre intended for the demonstration of passive load alleviation was the pull-up-push-over manoeuvre. This manoeuvre was primarily chosen for its symmetry. Unlike the sustained turns at constant bank angle, the pull-up-push-over manoeuvres are symmetric with respect to the longitudinal plane which results in equal loading of both port and starboard halves of the wing. In this sense the pull-up-push-over manoeuvre much better reflects the load cases and the modelling approach used during the design of the reference and the tailored wings. In addition to symmetry, the pull-up-push-over manoeuvre also generates a very clear increase in load factor which is easy to detect in the recorded flight test data.

The pull-up-push-over manoeuvre was defined using the flight dynamic model of the aircraft in reference configuration (equipped with reference wing). Several manoeuvres were simulated by first trimming the aircraft in level flight at given flight velocity, followed by a constant rudder deflection for two seconds as shown in Figure 8a. The average and the maximum load factors were extracted from the simulated responses and the elevator-per-g stability derivative of the aircraft was determined as shown in Figure 8b. The results indicate that the peak load factor is significantly higher in comparison to the average load factor for rudder deflections beyond ± 3 deg. For the sake of safety, it was decided to estimate the elevator-deflection-per-g characteristic based on maximum load factors. The procedure was repeated for several flight velocities as shown in Figure 9 and the acquired characteristics were used to evaluate several pull-up-push-over manoeuvres as summarized in Table 6.

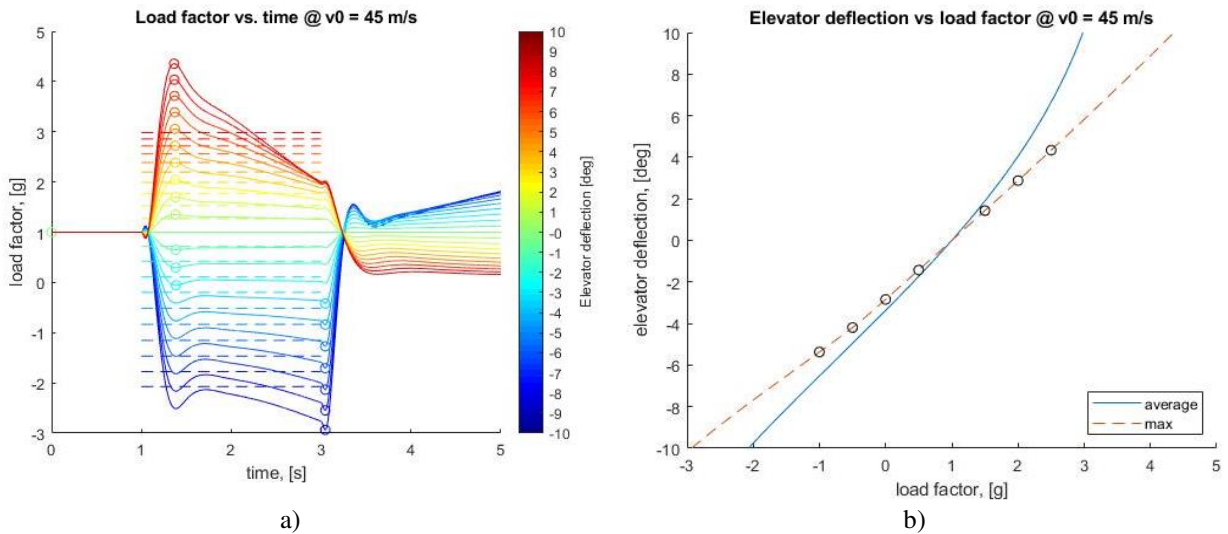


Figure 8 : Load factor vs. time, a), and elevator deflection vs. load factor, b), at $v = 45 \text{ m/s}$

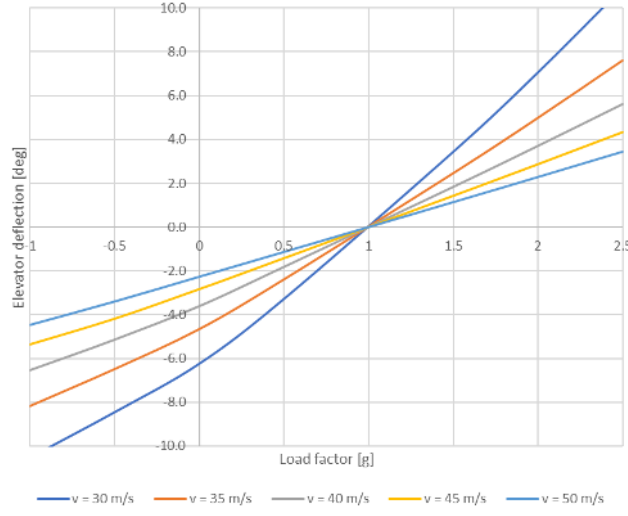


Figure 9 : Elevator deflection vs. maximum load factor for various flight speeds

Table 6: Required rudder deflections for pull-up-push-over manoeuvres

load factor, [g]	Elevator deflection* [deg]				
	$v = 30 \text{ m/s}$	$v = 35 \text{ m/s}$	$v = 40 \text{ m/s}$	$v = 45 \text{ m/s}$	$v = 50 \text{ m/s}$
-1	-10.5	-8.2	-6.5	-5.4	-4.5
-0.5	-8.5	-6.5	-5.2	-4.2	-3.4
0	-6.2	-4.7	-3.6	-2.8	-2.3
0.5	-3.3	-2.4	-1.8	-1.4	-1.1
1.5	3.4	2.5	1.8	1.4	1.1
2	7.1	5.0	3.7	2.9	2.3
2.5	10.9	7.6	5.6	4.3	3.5

*positive angle = elevator deflection upwards

In addition to elevator input, the manoeuvre distance had to be evaluated to ensure that it fits within the designated flight perimeter and altitude boundaries. Therefore, a hypothetical manoeuvre flightpath was assumed as depicted in Figure 10.

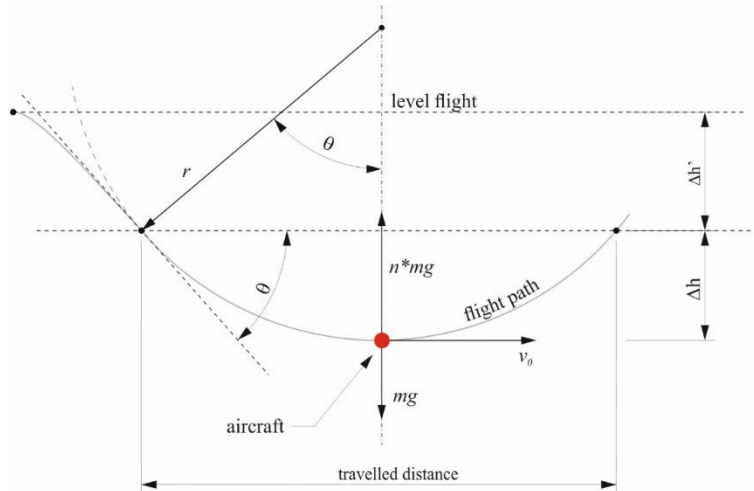


Figure 10 : Assumed flight path of the pull-up-push-over manoeuvre

The radius of the pull-up-push-over manoeuvre is estimated based on the selected load factor and flight speed. Once the manoeuvre radius is known, the change in altitude, the horizontal distance travelled, and the time of the manoeuvre can be determined. An overview of the manoeuvres performed at flight speed $v = 45\text{m/s}$ is given in Table 7.

Table 7 : Evaluation of pull-up-push-over manoeuvres

Load factor [g]	θ [deg]	r [m]	Δh [m]	t_{man} [s]	d_{man} [m]
1.5	30	413	55	9.6	413
2	30	206	28	4.8	206
2.5	30	138	18	3.2	138
3	30	103	14	2.4	103

After the theoretical evaluations of the pull-up-push-over manoeuvres the following procedure for the pilot was developed:

1. Trim at 40m/s.
2. Pull-up slightly to drop the speed to 35m/s.
3. Pushover until flight path angle was around -30deg.
4. When 45m/s is reached, pull-up with constant elevator angle.
5. When aircraft decelerates to 30m/s, level out.

This had to be done with pilot not knowing the elevator deflection nor the flight path angle, because the manoeuvre was too fast for the information to be communicated from the ground control station. However, the resultant data was of good quality and several of such manoeuvres with load factors ranging from -1 to +3 were achieved.

B. Fiber Bragg Grating System Layout

The load alleviation and flutter suppression mechanisms developed in the context of FLEXOP are to be assessed via the calculation of in-flight wing shapes and loads. The quantities of interest are vertical deflection, torsional twist, bending moment and shear force. The baseline (-0) and tailored (-2) wings are equipped with Fiber Bragg Grating (FBG) strain and temperature sensors, to provide the reconstruction data.

Preceding work focused on the development and assessment of the theoretical methods for wing shape and load calculation [6], as well as the calibration and validation of the measurement system [11], prior to use in flight. This section therefore only gives a short overview of the FBG system layout. The focus is then on the acquisition and processing of flight data, and finally the reconstruction and assessment of the loads and shapes, for selected flight maneuvers presented in chapter IV.B.

The strain FBGs used for the monitoring of the wings form two sensor configurations based on their positioning on the skins of the wings. The two configurations, along the axis (both pairs) and spars (-2 only) respectively, are shown in Figure 11. The former is designed to measure both shapes and loads, using 20 rosettes at both skins. The latter, consisting of 8 FBGs per skin, per spar, is an alternative approach to shape sensing alone, using significantly fewer FBGs. In addition, 10 temperature FBGs per skin are included along the wing axis for correction from thermal strains. The fibers are connected to 4 interrogator (“gator”) units in the fuselage, for raw data acquisition.

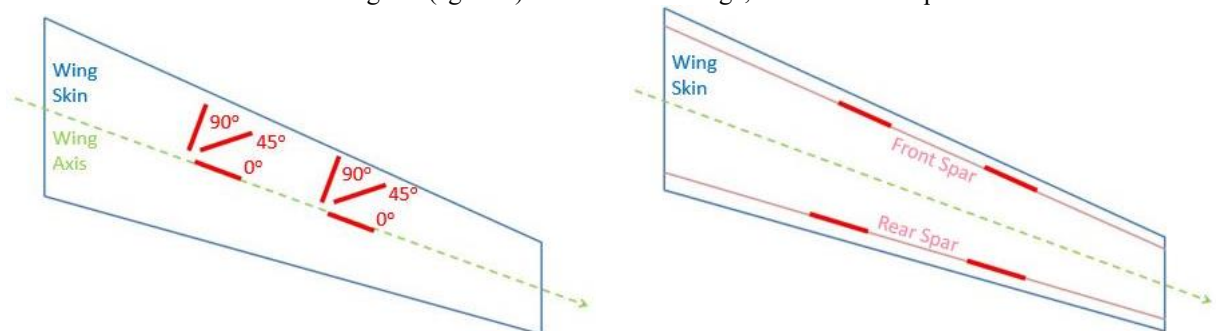


Figure 11: FBG configurations along the axis (left) and spars (right)

C. Baseline Flight Controller and Accelerometers

The main objective of the designed Flight Control Computer (FCC) is to give reference signals for the actuators and read the onboard sensors to provide feedback for the baseline controller. The high system frequency of 200Hz allows data acquisition for model identification and the control system. The recorded sensor data can be used by the autopilot, saved to logfile or partially streamed to the ground.

There is a main IMU and GPS unit in the fuselage called xSens for general purposes. Flutter is detected by dedicated flutter IMUs which were custom designed.

1. IMU Measurement system

The sensors were positioned according to their locations in the design on Figure 12, inside all three kinds of wing, to have commonality and comparison possibility in the models.

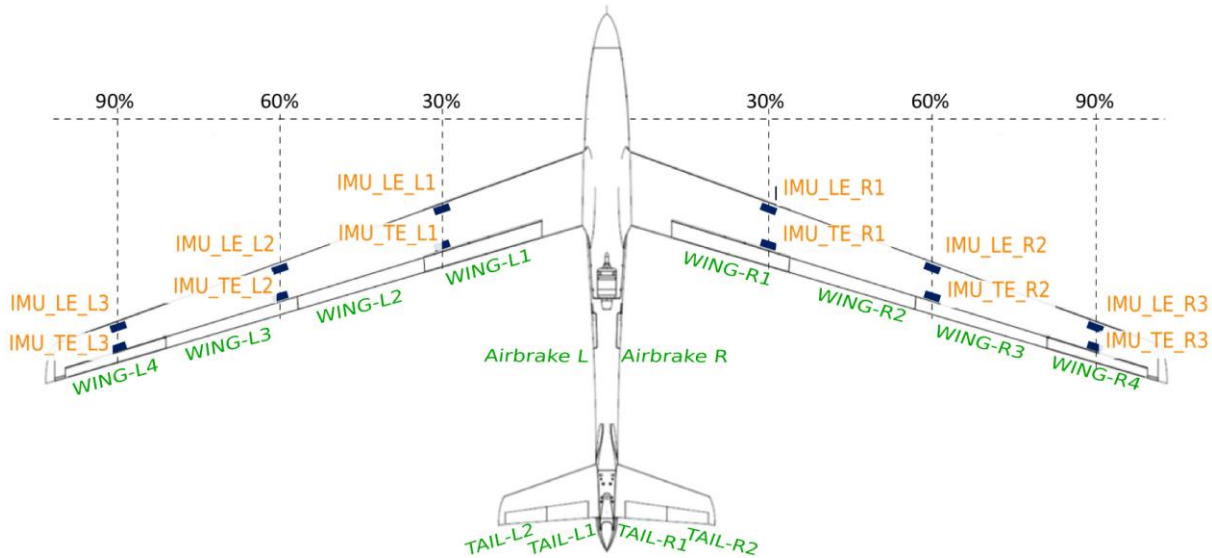


Figure 12 : Placement of flutter IMUs inside the wing

IMUs can provide inertial measurements to monitor the wing during flight and detect flutter. During wing manufacturing, IMUs were glued in the wing, the cable routing was made, and the wing was then closed permanently. Afterwards, hardware modification is not possible, thus a redundant system was designed: there are two fully independent IMU circuits on one PCB, one on the top and another on the bottom side. On Figure 13 the top part can be seen. IMUs send their measurements to the flightHAT (interface panel of the FCC). There are two CAN bus on a wing, called as top and bottom, working fully separately, one side can be used at a time, the other side acts only as a cold reserve. If a device on either bus fails, the other bus can be plugged in and used hereafter. If software modifications are necessary in the IMU software, a bootloader can be used for device programming.

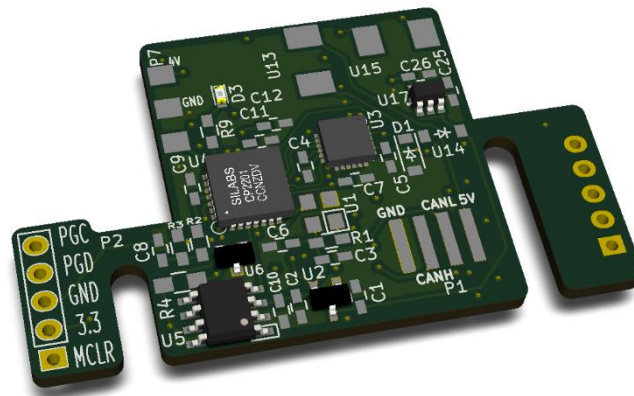


Figure 13 : A flutter IMU board

The IMU features a MPU6000. This sensor is a digital 6 degrees of freedom sensor. It is capable of measuring the acceleration up to +/- 16g and the angular velocity up to +/- 2000/s. The access to the measured data proceeds via SPI communication and the sampling rate is 1 kHz. An additional sensor AD2286 is an acceleration sensor only. This device is used for measure the acceleration only in z direction in greater range (up to +/- 70g). It is an analog sensor with proportional voltage output to the current acceleration. To measure the actual acceleration, the microcontroller uses its internal 12 bit analog-digital converter. The sampling rate from this device is synchronized to the 1 kHz sampling rate of MPU6000 Figure 14.

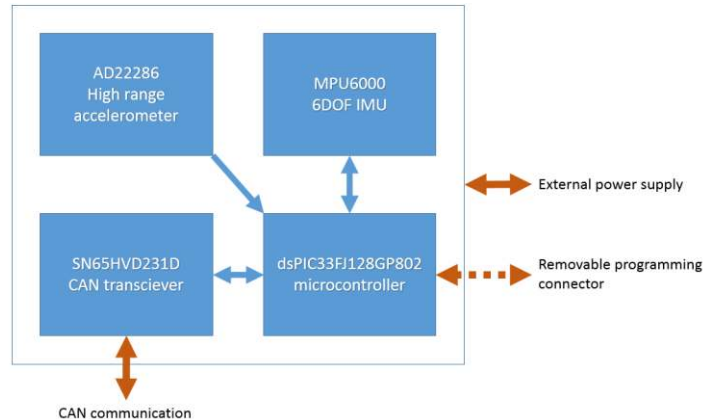


Figure 14 : IMU hardware layout

These sensors are connected to the main control computer system (FCC) via CAN bus and sending the measurements with 200Hz to the flightHAT board. This is the I/O extender and data flow control system of the FCC. It forwards the collected sensor data, including the IMU and xSens data, to the Raspberry PI via SPI communication which is main processing unit. It has 3 threads running in real time: Logging and Telemetry are subordinated to Control thread. The baseline controller is running in the Control thread, and implemented in MATLAB Simulink.

The sensor data used by autopilot is filtered non-linearly to avoid high spikes, and invalid data samples. A log thread saves the sensor data into the log file at 200Hz frequency for later analysis. The telemetry thread can send some data to Ground Control Station for human supervision or for further processing.

2. Baseline Flight Controller

The aim of the baseline controller is to augment the rigid body motion of the aircraft features. For sequential testing purposes a classical cascaded flight controller architecture was selected with gain-scheduled control loops [15],[16]. The controller provides augmented flight capabilities with a pilot in the loop as well as full autonomous flight capabilities. Three different modes of controlling the aircraft are considered in the flight control system:

- **Direct Mode:** The direct mode allows the pilot to bypass the flight control system. The only part in the flight control computer is the mapping from the received remote-control signals to the commanded surface deflections. The pilot controls the pitch, roll and yaw axis via the surface deflections and the aircraft speed via the thrust setting.

- **Augmented Mode** The augmented mode switches on basic augmentation for the pilot. Instead of directly controlling the surfaces, the pilot commands are transferred to pitch and roll attitude commands. The side slip angle is automatically commanded to zero, reducing the pilots need to control the yaw axis separately. Speed control remains in direct control, i.e. the pilot controls the speed via the thrust setting on.

- **Autopilot Mode** In this mode the pilot fully delegates the aircraft control to the FCS. Altitude, course angle, speed and side slip are automatically controlled. To be able to fly along the defined test pattern, reference commands based on the aircraft position are generated in a navigation module.

To facilitate the control design task and allow for the aircraft control modes (ii) and (iii), a series of cascaded control systems, illustrated in Figure 15 are used. As the cross coupling between longitudinal and lateral axis is negligible, longitudinal and lateral control design is separated. Thrust commands δ_{th} which are transferred to an engine revolution

command δ_ω via a nonlinear mapping and the elevator δ_e are the available actuators for longitudinal control. Lateral-directional control generates aileron (δ_a) and rudder commands (δ_r).

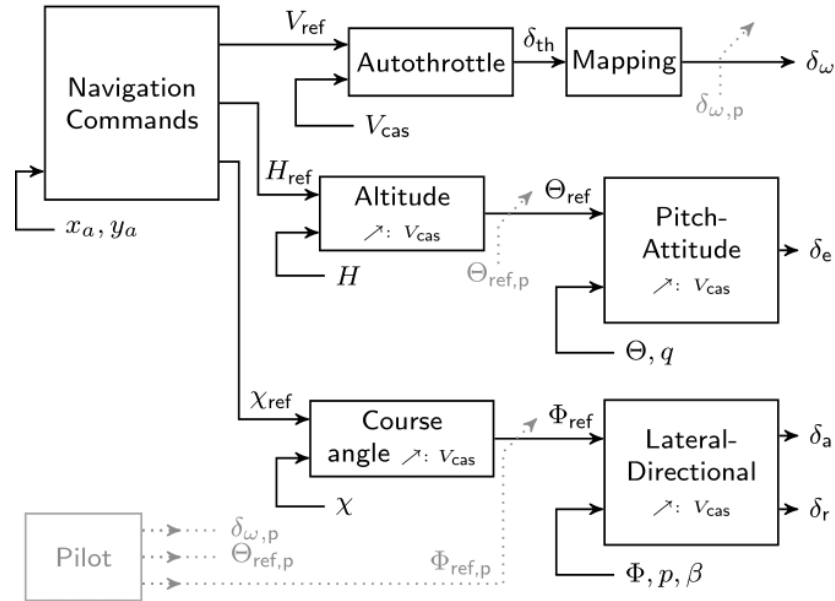


Figure 15 : Control architecture for fully automated flight (mode (iii)), and augmented flight (mode (ii)), indicated in gray.

The inner loops provide the basic augmentation to achieve uniform flying qualities over the whole speed range. These loops are the found the basis for the augmented mode (ii) to assist the pilot in flying the aircraft using the remote control. Also, the inner loops are the first cascade of the autopilot functionalities.

Pitch-Attitude Control

The pitch-attitude controller is used in the inner loop to allow the pilot to control the visible pitch attenuation of the aircraft. This is an intuitive control strategy for the pilot as the aircraft's orientation is directly controlled. A proportional-integral controller (PI) is used to ensure zero steady state error. Additionally, a pitch damper via a feedback of the pitch velocity q ensures adequate damping of the short period mode of the aircraft. All controller gains are depended on the aircraft's velocity to ensure adequate control performance over the whole speed range. Adding an additional roll of filter is crucial for the design of the inners loops to ensure the frequency separation to the flutter controller as well as avoid an excitation of lightly damped modes by the baseline controller in any case.

For the design of the pitch-attitude control gains a model matching approach is chosen. The desired tracking model is defined in terms of a second-order system with a minimum damping ration of 0.6 and corresponding frequency. Additionally a minimum phase margin of 45 degrees is defined to ensure satisfactory robustness. Parametric structured controller design problem is solved to obtain the corresponding gains, with quadratic dependence on V_{ias} .

Lateral-Directional Control

The lateral direction of the aircraft is controlled via the rudder and aileron deflections. The pilot is able to command the roll angle of the aircraft Φ and thereby directly control the aircraft's orientation. Additionally, the stick zero potion thereby corresponds to a wing level command, i.e. the aircraft flying straight. To provide sufficient roll damping, a roll damper is added to the controller, depending on the aircraft's velocity in a linear fashion.

Note that through the free integral in the aircraft dynamics a proportional feedback of the roll rate ensure also zero steady state error for roll attitude commands. As for the longitudinal loop, an additional roll of filter with a bandwidth of 25 rad/s is added after the control gains.

To optimize the parameter dependent controller gains, the structured controller design problem is solved. Similarly to the pitch-attitude loop, two requirements are used. A response time of 1 s with steady-state error of 0.1 degrees is defined for the tracking behavior. Additionally, 45 deg of phase margin are defined.

To enable coordinated turn maneuver with a zero side-slip angle, the side-sleep angle β is controlled to zero via the gain scheduled PID controller. The derivative is approximated using a first order derivative, with a time constant $\tau_d =$

0.1 s. The coordinated turn capabilities specially help the pilot to fly through turns much easier, as direct relationship between the orientation of the aircraft and its flight direction is ensured. In order to achieve this the gains of the side-slip loop were tuned for satisfactory disturbance rejection behavior.

The outer loops of the control system allow to fly the aircraft fully autonomously, which is required during the flutter tests. For the flight controller in this paper the altitude and speed for the longitudinal dynamics and the flight direction for the lateral directional dynamics are chosen to be the controlled variables.

Autothrottle

The speed controller features a constant (Linear Time Invariant) two-degree-of-freedom (2-DOF) PID loop and a non-linear mapping. The feed-forward term is introduced in order to explicitly consider the low bandwidth of the jet engine and the effect of the engine's time delay for the reference command channel. In other words the controller speeds up the response to reference changes without decreasing the robustness. The derivatives of the reference speed and the feedback signal are approximated by first order derivative filters of the form $\frac{s}{\tau_d s + 1}$ with a time constant $\tau_d = 0.01$ s. The presented 2DOF-PID autothrust controller provides the required thrust δ_{th} , which is mapped to the required revolution-speed command δ_ω received by the engine. Thus, the presented controller is extended by the non-linear mapping, realized via a lookup table in the controller.

Due to the complexity of the engine and the speed feedback loop, a direct numerical optimization is selected for tuning the corresponding gains. A simulation-based approach is applied to solve the design problem and find the constant gains. In the optimization, the gains which minimize the quadratic error between the reference speed and the response of the non-linear model are determined.

Altitude Control

The outer loop for the longitudinal motion of the aircraft features an altitude reference command system. Holding the reference altitude command is crucial during the operation as any speed increase due to altitude loss needs to be avoided due to the flutter effects, which appear at high speeds. Here, a gains-scheduled PI controller is selected. To determine these gains, the structured controller design problem is solved. For the altitude tracking, a bandwidth 5 times below the resulting inner loop pitch response is desired. A factor of 5 is considered to provide a sufficient frequency separation within a cascade controller design.

Course Angle Control

To allow the tracking of way-points, a flight direction control is implemented as outer loop for the lateral control of the aircraft. Controlling the course angle χ also has the great advantage that the effect of wind effects can be compensated, and the drift of the aircraft can be reduced [15],[16]. The flight direction controller is derived a parameter depended PID controller. All of the controller gains are depending quadratically on the scheduling parameter V_{ias} . The inclusion of a derivative term in the controller structure ensures a fast (input) disturbance rejection. Again, the derivative term is replaced by a first order derivative filter, with a time constant $\tau_d = 0.1$ s. The roll angle command Φ_{ref} is additionally filtered using a second order filter to improve the noise attenuation in the course angle feedback signal.

The gains of the course angle controller are determined by demanding a response time of 5 s, which is five times slower than the roll loop, in a model matching setup. Again, a quadratic dependence on V_{ias} is selected for the controller gains.

The navigation system generates the command signals for the flight control system allowing to navigate the aircraft around a predefined flight test pattern. Thus, a level above the basic flight controllers (see Figure 4) a state machine generates these required commands depending on the actual longitudinal (x_a) and lateral (y_a) aircraft positions in the earth fixed frame.

IV. Flight Test Results

A. Evaluation of Aeroelastic Manoeuvres

In the course of the flight test campaign there were several sustained turns with constant bank angle and pull-up-push-over manoeuvres executed. So far, these manoeuvres were assessed for quality in terms of how constant were individual manoeuvre parameters, such as load factor, bank angle, and flight speed, during the execution of the manoeuvre. Both sustained turns as well as pull-up-push-over manoeuvres were executed with both the reference and tailored wings.

An example of raw recorded data is shown in Figure 16. The pull-up-push-over manoeuvres are clearly visible in the time interval between 1180 s and 1400 s by looking at the second subplot depicting vertical acceleration (in body coordinates) a_z in blue. The sustained turns are also clearly visible in the time interval between 1500 s and 1800 s by looking at the last subplot depicting yaw angle (in earth coordinates) in red. One can also clearly observe the increasing rate of turn with increasing roll angle of the aircraft which indicated by the red line in the second subplot.

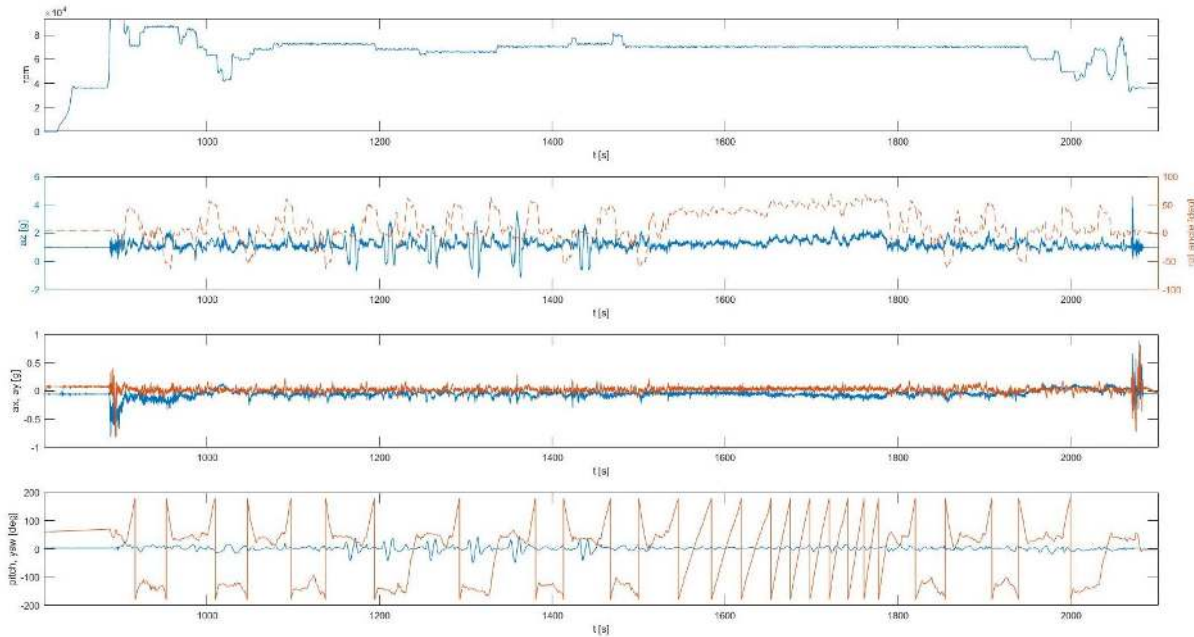


Figure 16 : Time series of the flight test data

The pull-up-push-over manoeuvres are assessed first. The manoeuvres are extracted from the raw data and realigned as shown in Figure 17. One can see that the load factor and flight speed are constantly changing in the course of the manoeuvre. To be able to compare various manoeuvres and to eliminate short period oscillations it was decided to average the extracted data over the time interval of ± 1 s around the maximum load factor experienced during each manoeuvre as indicated by the grey averaging window in Figure 17b. All the manoeuvres for both the reference and the tailored wing were processed in this manner.

The processed manoeuvres are shown in terms of elevator-deflection-per-g characteristic in Figure 18. The error bars indicate standard deviation of either the rudder deflection angle and the load factor around their corresponding mean values. Furthermore, the labels indicate the manoeuvre ID number and the average flight speed of the manoeuvre. This way manoeuvres performed at similar flight conditions can be compared to each other. For instance, the manoeuvres 1,2,4, and 5 pertinent to the reference wing were executed at velocity of about 50 m/s. Hence, these manoeuvres can be fitted with a linear model in order to obtain the elevator-per-g stability derivative similar to that shown in Figure 9. The fitted model is indicated by the yellow line. Comparison to numerical values obtained using the flight dynamic model shows good agreement. The difference between the experimental and numeric values is 11% and 30% respectively for the stability derivatives obtained using average and maximum simulated load factors. The absolute values are also listed in Figure 18.

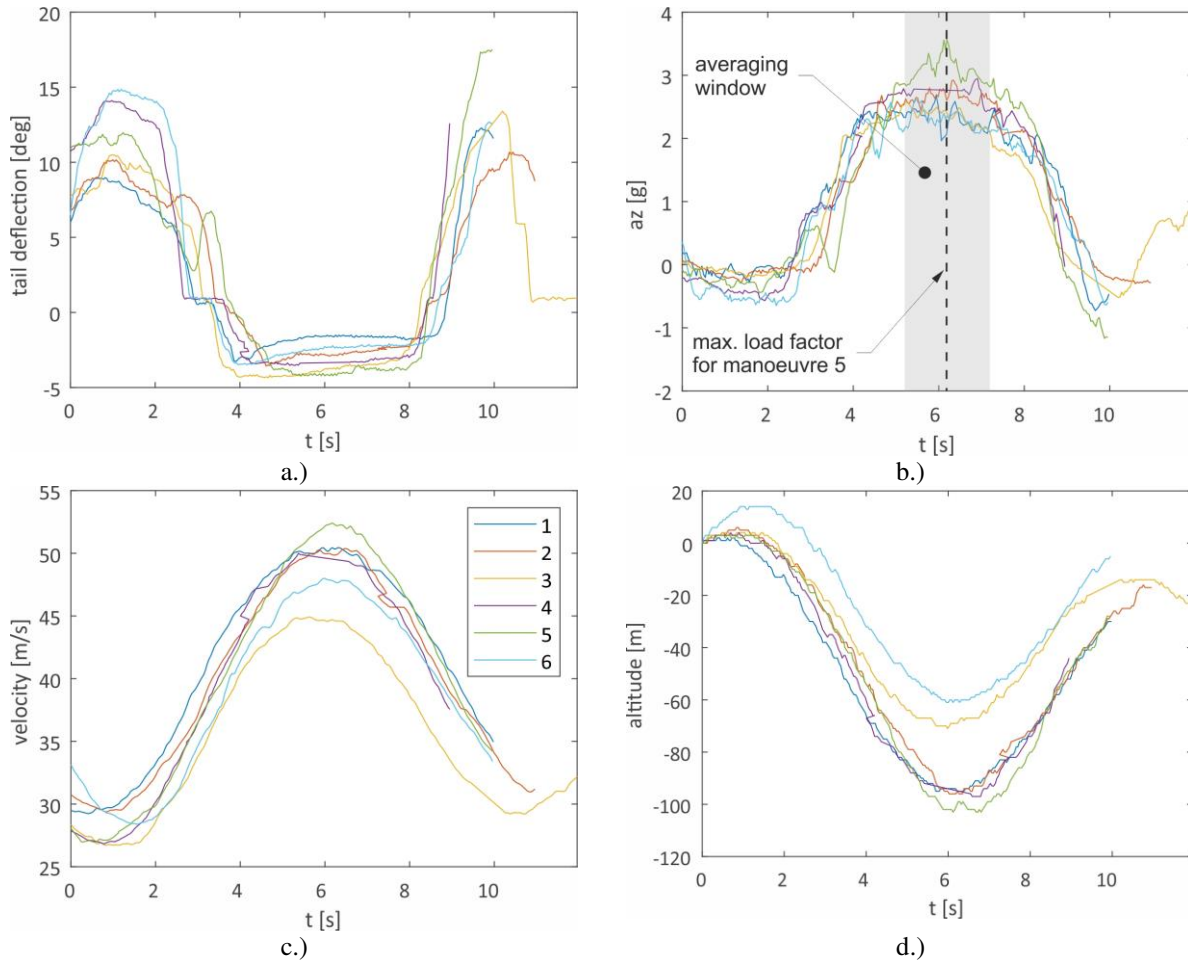


Figure 17: Pull-up-push-over manoeuvres for (-0) aircraft configuration

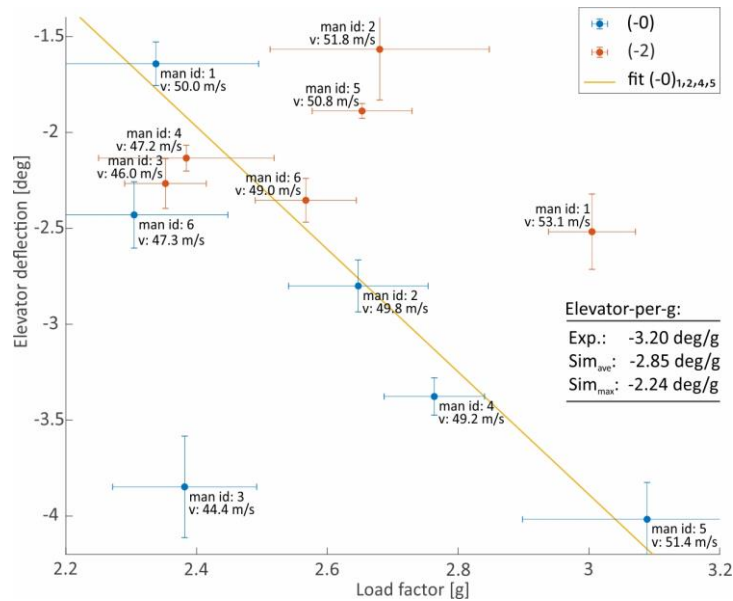


Figure 18 : Load factor vs. elevator deflection

Sustained turns at constant bank angle are considered next. Figure 19 shows the recorded flight data for bank angles of 40 deg, 50 deg and 60 deg for both the reference and the tailored wing. The increase in load factor with increased bank angle is evident in both data sets. The major difference between the two datasets is in the way the manoeuvres were executed. In the case of the reference wing, the manoeuvres were flown manually, while in the case of the tailored wing the autopilot was employed. Hence, one can observe a significantly reduced standard deviation in the dataset pertinent to the tailored wing. The usage of the autopilot also results in much better coordinated turn which is clearly visible from the difference in the amount of sideslip-angle present during the execution of the turns. In the case of the reference wing, the amount of sideslip was on average about -4 deg, while the average sideslip was only about -0.5 deg in the case of the tailored wing.

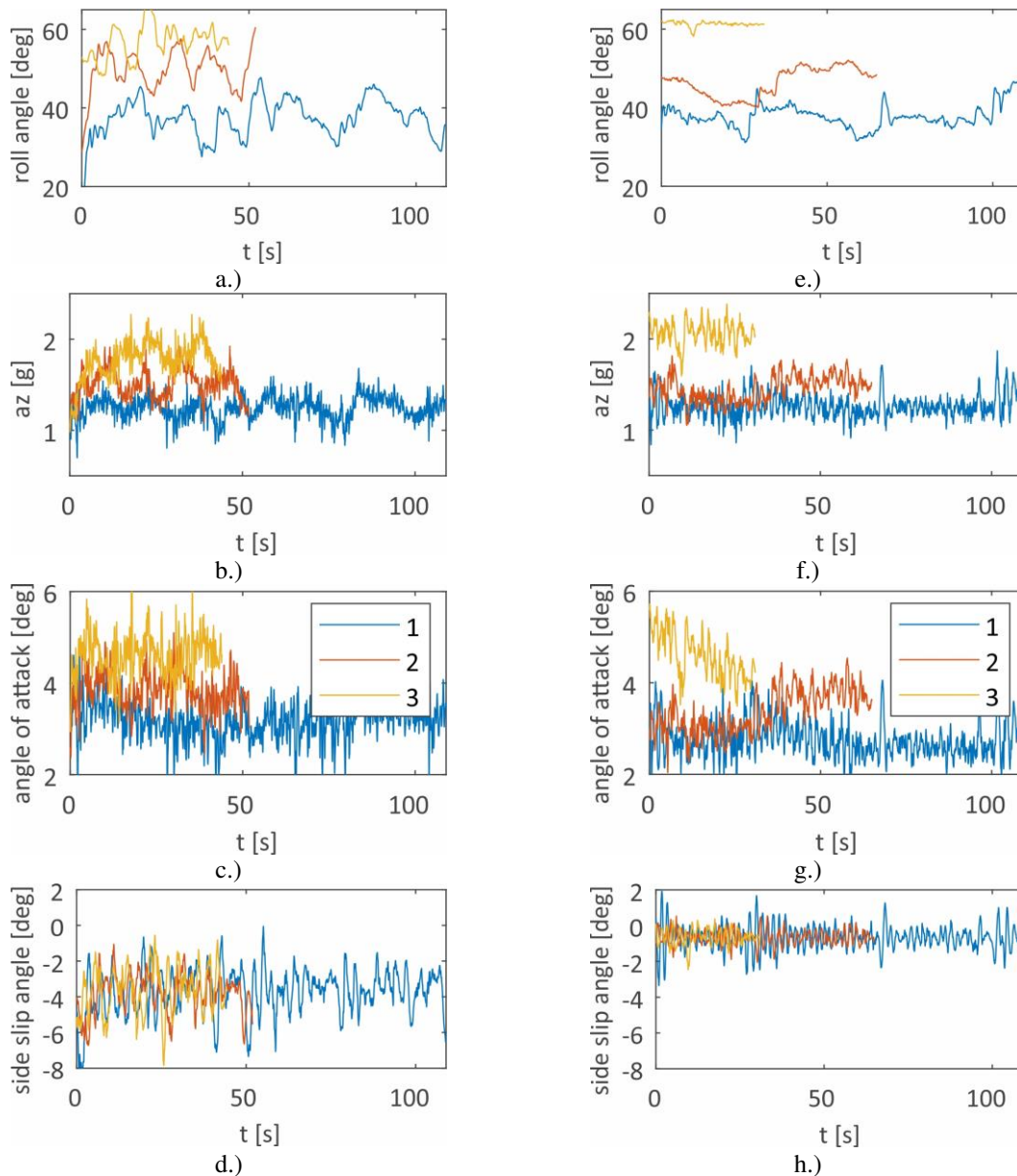


Figure 19 : Test flight data for (-0) aircraft configuration (left) and (-2) aircraft configuration (right) in sustained turn at constant bank angle

Similarly, to the pull-up-push-over manoeuvres, the measured bank angles and the load factors were averaged over the duration of the turn and compared against each other and to the theoretically expected value. The results are shown

in Figure 20. The load-factor-to-bank-angle relation for both the reference and the tailored wing follows very well the theoretically predicted behaviour which indicates the manoeuvres were well executed and that the expected load levels were achieved. The error bars indicate the standard deviation of the bank angle and load factor around their mean values. It is evident that the bank angle was much better controlled in the case of the reference wing due to the usage of the autopilot, which also results in significant reduction of the standard deviation in the measured load factors. Finally, in the case of the reference wing, the standard deviation in the measured load factor is increasing with increasing bank angle. That is expected since the sensitivity of the load factor to bank angle variation is increasing with increasing bank angle.

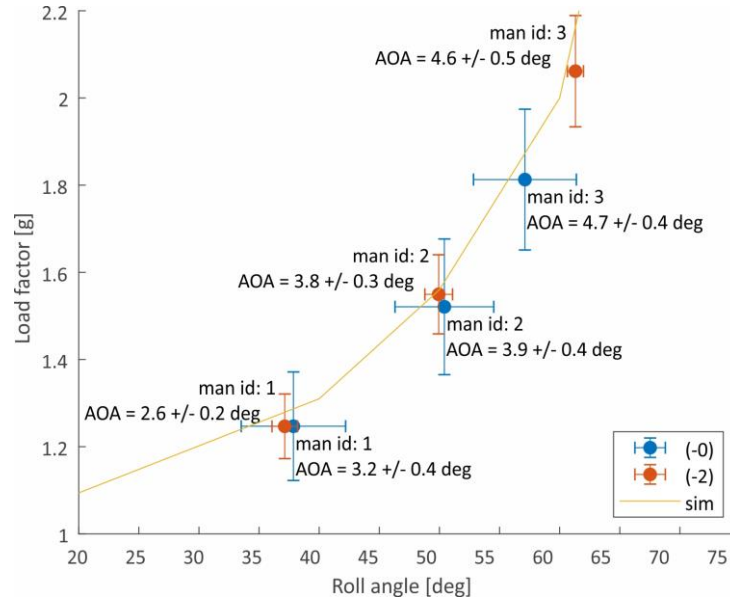


Figure 20 : Comparison of sustained turns at constant bank angle

B. Strain-Based Wing Shape & Load Reconstruction

1. Raw Data Acquisition & Processing

The -0 and -2 wing FBG monitoring system was operated in flight, yielding valuable strain and temperature data. Figure 21 presents the raw data measured by a 0° strain FBG and a temperature FBG on the lower wing skin of the left hand -0 wing, at approx. 2.9 m wing span, during Flight Test 4 (FT4). A focused view of a “pull-up” maneuver is also shown; load and shape reconstruction focuses on these maneuvers.

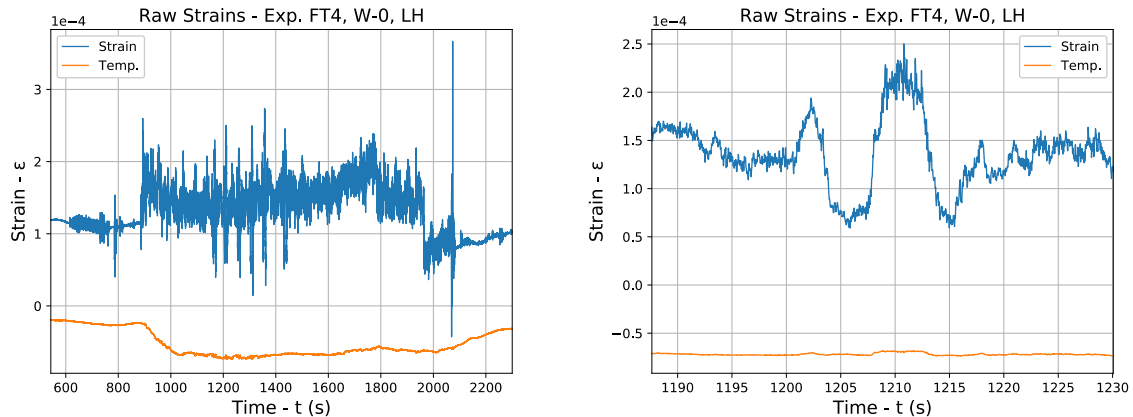


Figure 21: FT4 raw data from the full flight (left) and a pull-up maneuver (right)

The variation of temperature and its significant effect in strain measurement is evident from the graph above; the same holds for the low frequency, non-periodic “drift error”, whose presence was discovered during ground testing, corrupting calibration data. Another interesting finding is the maintenance of temperature at constant levels during flight and especially throughout the duration of a maneuver (approx. 30 s).

An approach was developed for the extraction of flight strains from raw data, corresponding to individual maneuvers, based on the wing loading conditions measured from other monitoring systems installed on the aircraft. Consequently, limitations imposed by imperfect calibration of the system, along with the presence of thermal and drift error strains, were overcome. The approach is based on the following two assumptions:

A1. Constant Drift Error & Temperature: These two sources of error are assumed constant over the duration of a pull-up; consequently, the evolution of strains remains unaffected.

A2. Accurate Numerical Calculation of Gravitational & Aerodynamic Loads: Assuming these are the only two loads acting on the wings, the corresponding strains can be calculated numerically. A gravity load case can be applied in the Finite Element (FE) model of the wing, yielding the “gravitational strains”. Previous Computational Fluid Dynamics (CFD) studies have also calculated numerical estimates of lift, for several combinations of load factor, airspeed and fuselage mass; by treating lift as a set of point forces, the equivalent “lift strains” can be found.

Ultimately, the two assumptions suggest that the correct flight strains can be extracted, given a short period of known loading conditions during the maneuver. Hence, pull-ups were modified to include a 5 s segment of steady 1G flight at the onset of the maneuver. The corresponding airspeed and fuselage mass are calculated, and hence the lift distribution is computed, from the CFD analysis. Additionally, the raw strain profile is normalized, keeping the “pull-up strains”. Using correction factors, the numerical gravitational and lift strains are expressed as FBG strains and added to pull-up strains, finally yielding the flight strains. Figure 22 presents the above concept, showing how Flight Control Computer (FCC) and gator data are used for the processing of raw flight strains, for a FT4 pull-up.

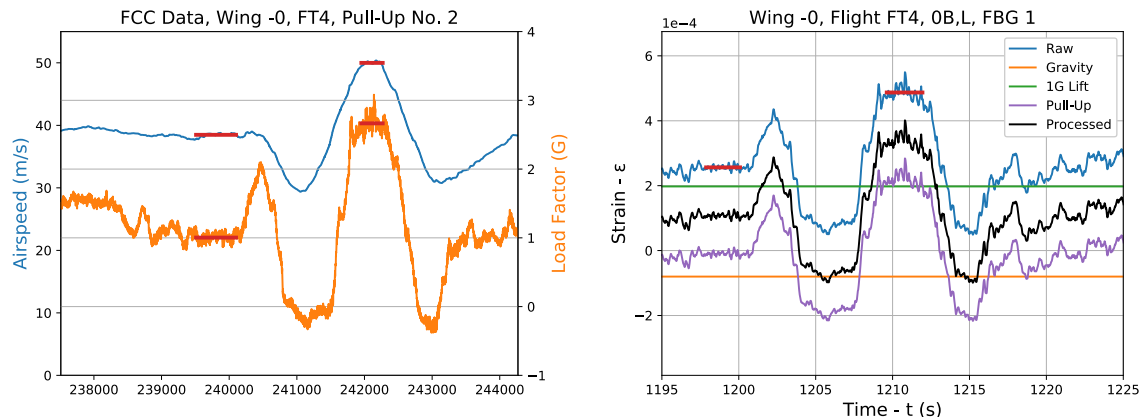


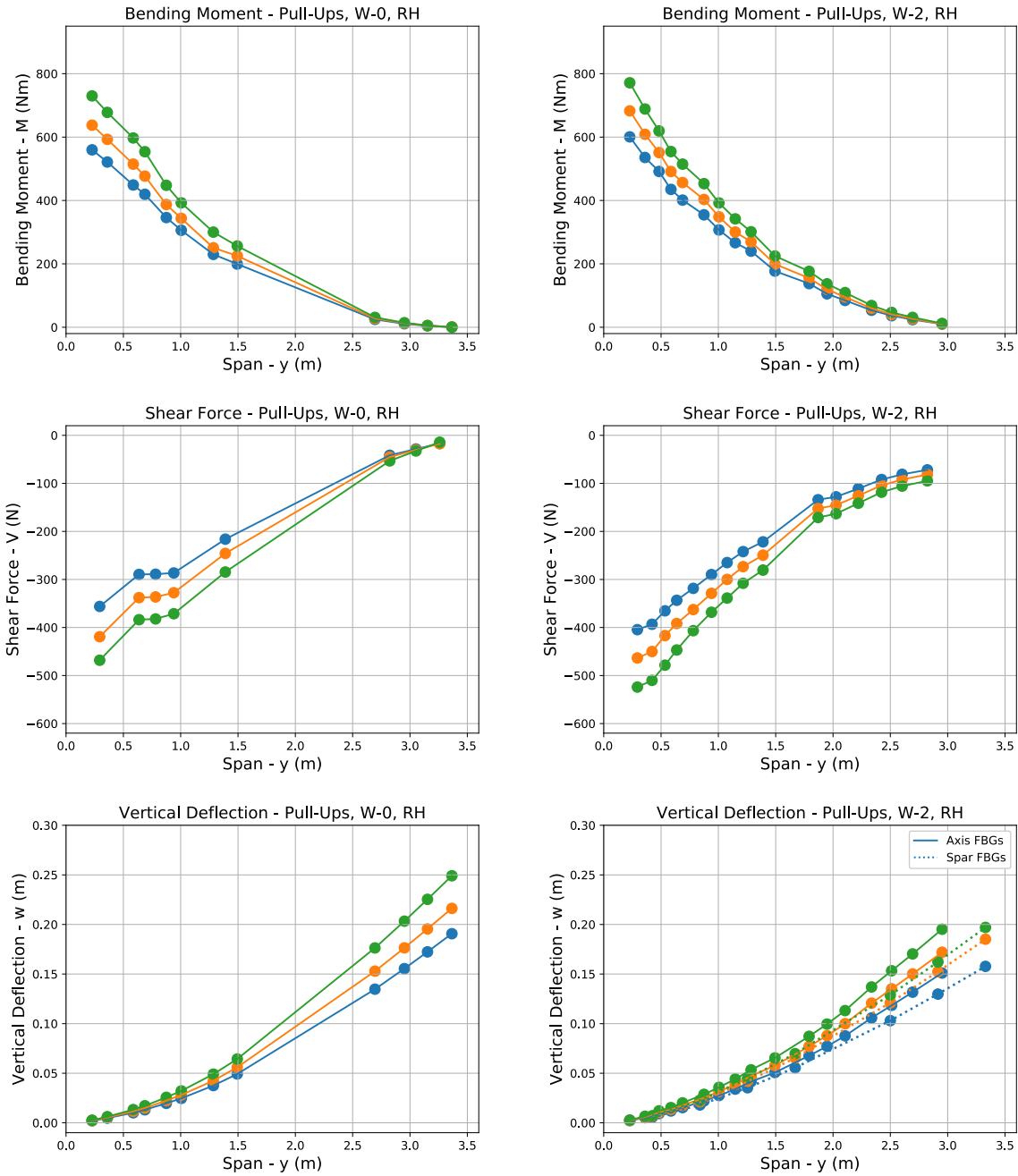
Figure 22: Calculation of correction parameters (left) and flight strain extraction (right)

The reconstructed pull-up results refer to the “peak” (approx. from 1209 to 1212 s in Figure 22) of the maneuver. A good correlation between raw strains and load factor can be observed in the respective distributions; thus, the measurement system’s ability to capture dynamic strains is further validated. Due to challenges in manual aircraft control, wing vibration is significant in that region, adding some uncertainty to the calculation of the corresponding strain and load factor. No obvious correlation was observed between measured strains and airspeed.

2. Flight Load & Shape Reconstruction

Upon the extraction of flight strains the reconstructed pull-up load (bending moment (M), shear force (V)) and shape (vertical deflection (w), torsional twist (ϕ)) results were calculated for -0 and -2 wings, using the relevant load and shape sensing parameters [6]. As found in previous studies using ground test data, torsion moment (T) was not possible to resolve due to the dominance of bending in the applied loading, and is therefore not presented. In addition, the limited number of FBG readings during the flight tests did not allow a good reconstruction of spar ϕ , which is also not presented.

Figure 23 presents selected reconstruction results along the wing span (y) for -0 and -2 right hand wings, corresponding to 3 maneuvers of different load factor, specifically 2.34 G, 2.67 G and 3.16 G for -0 and 2.37 G, 2.62 G and 3.03 G for -2 respectively, corresponding to the blue, orange and green lines. The graph of w for the -2 wing includes reconstructed results from both FBG configurations.



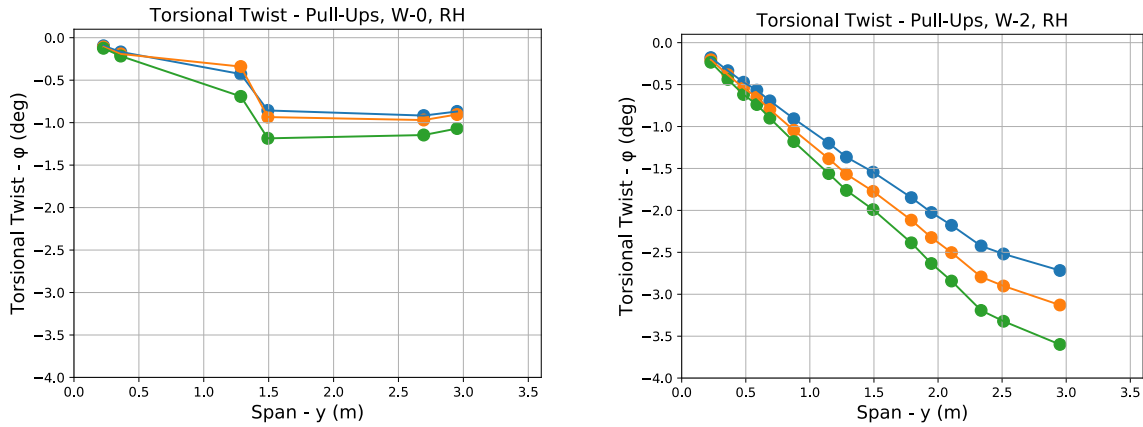
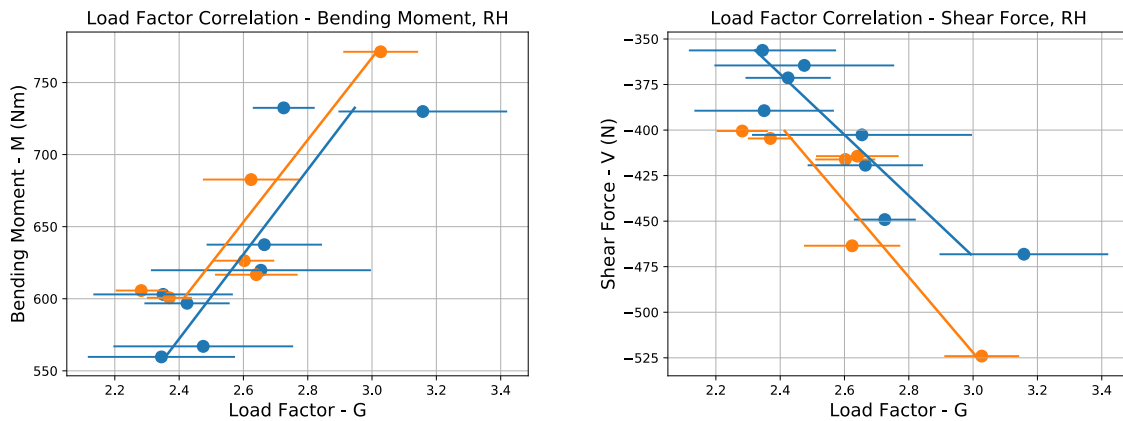


Figure 23: Reconstructed loads and shapes for the -0 (left) and -2 (right) wings

Overall, the loads and shapes are reconstructed with good accuracy, the lines and actual values being in accordance with numerical predictions. In addition, the system performed according to its known strengths and weaknesses, previously identified during ground testing. Specifically, M and axial w are reconstructed well [6] for both wings, despite the loss of many FBGs in -0. Similarly, though more sensitive to noise (especially in -0), V is also calculated accurately [6]. This is not the case with spar w , which was found using only 7 FBGs and was underestimated; ground testing results also showed this tendency, however to a smaller extent, its origins being under investigation. Finally, with regards to axial ϕ , the large order of ϕ calculated in -2 wing is of great interest, indicating the decreased torsional stiffness of the wing and the bending-twisting coupling effect due to the use of unbalanced laminates. The quality of the reconstruction depended on the number of 45° FBG readings collected during flight, which is evident in Figure 23, where the reconstruction was made using 6 and 15 sensors, for -0 and -2 wings respectively; this dependence was also foreseen by previous studies.

A total of 8 pull-ups were performed using -0 wings (FT4, FT5) and another 6 using -2 wings (FT6). Apart from the spanwise distribution, loads and shapes are particularly interesting close to the wing root and wing tip respectively. Figure 24 shows the reconstructed values at the corresponding locations, relative to the measured load factor. Due to the lack of FBGs at these particular locations, M is calculated at $y = 0.227$ m, V at $y = 0.290$ m and w, ϕ at $y = 2.951$ m. Horizontal error bars (standard deviation) are added to denote the uncertainty in the calculation of load factor. For the sake of comparison, only axial w is plotted for the -2 wing.



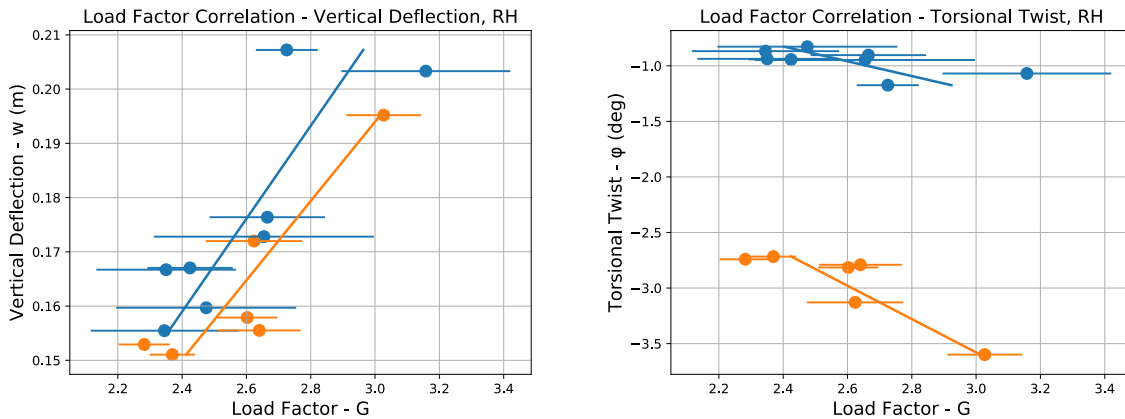


Figure 24: Load values at wing root (top) and shape values at wing tip (bottom) for -0 (blue) and -2 (orange) wings

Some interesting conclusions can be drawn from the graphs above. First of all measured values have a direct correlation with the load factor as anticipated. The lines in the graphs of Figure 24 are linear fits of the data and used mainly for visualization purposes. The exact correlation of each value with the load factor requires additional experimental data and thus more flight tests. Generally, the lines are indicative of the performance of each pair of wings. In terms of shapes, the findings are in good agreement with simulation and ground testing results, predicting slightly smaller w but significantly larger ϕ for -2 wings. The large ϕ calculated during flight, validates the use of unbalanced laminates in the design of wings. With regards to loads, similar root M and slightly greater root V are experienced by -2 wings. A possible explanation for the increased shear force is the addition of weights in the fuselage, to achieve the same take-off weight, using the lighter -2 wings. Roughly, this would result to the same total lift force, but decreased gravitational force and ultimately an increased shear force experienced. However, it must be noted that the calculation of V is known from previous studies to be sensitive to the accuracy of M , making it prone to random error.

The size of the error bars indicates the uncertainty present in the calculation of the load factor. In addition, deviations from the line are also attributed to secondary parameters such as airspeed, fuselage mass, angle of attack and the lift force experienced by the tail, to name a few. In the case of FBG readings of smaller magnitude ($< 10\mu\epsilon$), the effects of temperature and drift error can also be present. Overall, given the small sample size (8 and 6 pull-ups), these factors have a significant effect on the fit, and further analysis of all the flight conditions, along with additional data is required to draw better conclusions.

V. Conclusion

The goal of the FLEXOP project is to develop methods and tools to design higher aspect ratio light weight wings with the enabling technologies of load alleviation and active flutter control. The methods and tools should be validated with flight data gathered from an unmanned demonstrator aircraft. In this paper the flight test campaign and load alleviation manoeuvres together with the sensors for data acquisition as well as the concept of the autopilot for conduction precise tests are described.

In total, six test flights were performed up to date, providing 114 min of flight test data: 92 min with the baseline rigid wings -0 and 22 min with the load alleviation wing -2. First results of the flight test data evaluation are presented:

The elevator-per-g stability derivative was calculated from the flight test data and compared to theory. The results did match very well.

Furthermore a bending moment, shear force and wing shape comparison between the baseline and the load alleviation wing at different load factors has been shown. The FBG measurement system was operated reliably during flight, recording raw strain and temperature data for the -0 and -2 wings. In conjunction with FCC readings, the raw strains were corrected and finally used, along with the previously calculated load and shape sensing parameters, to calculate shapes and loads along the wing span. The reconstructed results are in accordance with predictions made using simulation and ground testing data. A correlation was observed between loads and shapes measured at the wing root and tip respectively with load factor, however more flight test data are necessary for a more detailed

characterization. Finally, the effects of load alleviation were confirmed experimentally, by the increased torsional twist, observed for -2 wings, confirming the use of unbalanced laminates for load alleviation purposes.

Acknowledgments

This project has received funding from the European Union's Horizon 2020 research and innovation program under grant agreement n° 636307.

References

- [1] Takarics, B., Patartics, B., Luspay, T., Bauer, P., Vanek, B., Roessler, C., Bartasevicius, J., Koeberle, S., Teubl, D., Hornung, M., Waitman, S., Marcos, A., Pusch, M., Wustenhagen, M., Kier, T., Looye, G., Meddaikar, M.: "Active Flutter Mitigation Testing on the FLEXOP Demonstrator Aircraft", AIAA Atmospheric Flight Mechanics Conference, AIAA SciTech Forum, Orlando, Florida, Jan.2019. (Submitted).
- [2] FLEXOP Consortium, "Horizon 2020: Proposal SEP 210181869 - FLEXOP," 2014.
- [3] "FLEXOP Project Homepage," <https://flexop.eu/news>.
- [4] Sodja, Jurij, Noud Werter, and Roeland De Breuker. "Design of a flying demonstrator wing for manoeuvre load alleviation with cruise shape constraint." 2018 AIAA/ASCE/AHS/ASC Structures, Structural Dynamics, and Materials Conference. 2018
- [5] M. Y. Meddaikar, J. K. S. Dillinger, J. Sodja, and R. De Breuker, "FLEXOP – APPLICATION OF AEROELASTIC TAILORING TO A FLYING DEMONSTRATOR WING," in DLRK 2018, 2018, pp. 1–10.
- [6] Roessler, C., Stahl, P., Sendner, F., Hermanutz, A., Koeberle, S., Bartasevicius, J., Rozov, V., Breitsamter, C., Hornung, M., Meddaikar, Y. M., Dillinger, J., Sodja, J., De Breuker, R., Koimtoglou, C., Kotinis, D., and Georgopoulos, P., "Aircraft Design and Testing of FLEXOP Unmanned Flying Demonstrator to Test Load Alleviation and Flutter Suppression of High Aspect Ratio Flexible Wings," in AIAA Scitech 2019 Forum, San Diego, California, 2019.
- [7] N. P. M. Werter and R. De Breuker, "A novel dynamic aeroelastic framework for aeroelastic tailoring and structural optimisation," *Compos. Struct.*, vol. 158, pp. 369–386, Dec. 2016.
- [8] R. De Breuker, M. M. Abdalla, and Z. Gurdal, "A Generic Morphing Wing Analysis and Design Framework," *J. Intell. Mater. Syst. Struct.*, vol. 22, no. 10, pp. 1025–1039, 2011.
- [9] J. K. S. Dillinger, T. Klimmek, M. M. Abdalla, and Z. Gurdal, "Stiffness Optimization of Composite Wings with Aeroelastic Constraints," *J. Aircr.*, vol. 50, no. 4, pp. 1159–1168, 2013.
- [10] Y. M. Meddaikar, F. X. Irisarri, and M. M. Abdalla, "Laminate optimization of blended composite structures using a modified Shepard's method and stacking sequence tables," *Struct. Multidiscip. Optim.*, vol. 55, no. 2, pp. 535–546, 2017.
- [11] Sodja, J., De Breuker, R., Meddaikar, Y. M., Dillinger, J. K. S., Govers, Y., Krüger, W. R., Georgopoulos, P., Koimtoglou, C., Roessler, C., Koeberle, S., Bartasevicius, J., Teubl, D., Gyulai, L., Toth, S., Nagy, M., Balogh, D., Jasdi, M., Bauer, P., and Vanek, B., "Ground Testing of the FLEXOP Demonstrator Aircraft", AIAA Atmospheric Flight Mechanics Conference, AIAA SciTech Forum, Orlando, Florida, 2020
- [12] Stahl, P., Sendner, F.-M., Hermanutz, A., Röbber, C., and Hornung, M., "Mission and Aircraft Design of FLEXOP Unmanned Flying Demonstrator to Test Flutter Suppression within Visual Line of Sight," 17th AIAA Aviation Technology, Integration, and Operations Conference, American Institute of Aeronautics and Astronautics, Reston, Virginia, 2017.
- [13] J. Sodja, N. Werter, and R. De Breuker, "Design of a flying demonstrator wing for manoeuvre load alleviation with cruise shape constraint," in 2018 AIAA/ASCE/AHS/ASC Structures, Structural Dynamics, and Materials Conference, 2018, no. 210049.
- [14] Y. M. Meddaikar, J. K. S. Dillinger, J. Sodja, and R. De Breuker, "FLEXOP – Application of aeroelastic tailoring to a flying demonstrator wing," in Deutscher Luft- und Raumfahrtkongress 2018, 2018, pp. 1–10.
- [15] R. Brockhaus, W. Alles, and R. Luckner. *Flugregelung*. Springer Verlag Berlin Heidelberg, 3 edition, 2011.
- [16] Brian L Stevens, Frank L Lewis, and Eric N Johnson. *Aircraft control and simulation: dynamics, controls design, and autonomous systems*. 2015.